Publication Year	2021
Acceptance in OA	2025-02-24T11:10:30Z
Title	Dissecting nonthermal emission in the complex multiple-merger galaxy cluster Abell 2744: Radio and X-ray analysis
Authors	Rajpurohit, K., VAZZA, Franco, van Weeren, R. J., Hoeft, M., BRIENZA, Marisa, Bonnassieux, E., Riseley, C. J., BRUNETTI, Gianfranco, BONAFEDE, Annalisa, Brüggen, M., Formann, W. R., Rajpurohit, A. S., Röttgering, H. J. A., Drabent, A., Domínguez-Fernández, P., Wittor, D., Andrade-Santos, F.
Publisher's version (DOI)	10.1051/0004-6361/202141060
Handle	http://hdl.handle.net/20.500.12386/36154
Journal	ASTRONOMY & ASTROPHYSICS
Volume	654

Table 7. Polarization properties of all four relics in the cluster Abell 2744.

Source	VLA		RM range	$\langle\sigma_{\rm RM}\rangle$
	S-band	L-band		
	$P_{3.0\,\rm GHz}$ (%)	$P_{1.5\,\rm GHz}$ (%)	(rad m^{-2})	(rad m^{-2})
R1	30 ± 4	19 ± 2	+1 to +19	5 ± 1
R2	34 ± 4	27 ± 3	+4 to +16	4 ± 1
R3	32 ± 3	13 ± 2	−2 to +18	6 ± 2
R4	25 ± 2	8 ± 1	–	–

Notes. The mean fractional polarization for the main relic R1 is measured from 10″ resolution image. We note that our S-band polarization value of R1 is slightly higher than those obtained by Pearce et al. (2017) because we measured polarization fraction from Faraday corrected S-band images. Since the polarized emission from the fainter relics R2, R3, and R4 are recovered well in low resolution images therefore, we report the mean fractional polarization measured from 15″ resolution maps.

radio halo, with a statistical measure of the significance of the correlation.

It is worth stressing that the strong/weak lensing analysis of Abell 2744 reveals a complex merger, involving at least four subclusters (Golovich et al. 2019). Subcluster 1 is elongated along the east-west direction, see Fig. 1. The X-ray data reveal an additional small northwest ICM component, close to the location of R3 (Fig. 1). Interestingly, regions following the anticorrelation belong to subcluster 1. A similar correlation has also been recently observed for the halo in MACS J0717.5+3745 (Rajpurohit et al. 2020b). The observed anticorrelation in the northern part of the halo implies that the faint X-ray regions show a steeper spectral index. This suggests that there is a steepening in the outermost regions of the halo. The spectral steepening in the outermost part of the northern part of the cluster is also evident in the spectral index maps shown in Fig. 9. Moreover, the data points that fall into the positive correlation belong to the subclusters 2, subcluster 3, and subcluster 4 (Fig. 1). In the next section, we discuss the presence of these two distinct components in detail.

6.3. Spatial correlation between spectral index and ICM temperature

We also compare the ICM temperature with the spectral index. We use the *Chandra* temperature map presented in Pearce et al. (2017). The resulting plot is shown in the right panel of Fig. 15. We again fit the data using `Linmix` to search for a possible correlation between spectral index and temperature. The Spearman correlation coefficient is 0.18. As found by Pearce et al. (2017), the relation between $\alpha - T_{\rm X}$ does not show any significant correlation.

Since in the $\alpha - I_{\rm X}$ relation, the halo shows two distinct trends, we also fit the data separately. As seen in the right panel of Fig. 15, in the northern part of the halo (subcluster 1) the flat spectral index regions seem to be associated with higher temperatures. For this region, we find that the Spearman correlation coefficient is $r_{\rm s} = 0.56$, indicating a moderate correlation between the spectral index and ICM temperature. Regions associated with the southern part of the halo (subclusters 2, 3, and 4) show relatively uniform spectral indices, namely between −1.0 and −1.25. The temperature in these regions varies from 3 to 7 keV.

To the best of our knowledge, the point-to-point correlation between the spectral index and ICM temperature has been quantitatively reported for one more halo, namely Abell 2255 (Botteon et al. 2020a). They found a hint of mild anticorrelation between the X-ray temperature and spectral index for the Abell 2255 halo. The moderate positive correlation between the spectral index and the ICM temperature for the northern part of the halo supports the idea that a fraction of the gravitational energy, which is dissipated during cluster mergers in heating the thermal plasma, is converted into reacceleration of relativistic particles and amplification of the magnetic field (Orrú et al. 2007).

The presence of two different clear trends in the $\alpha - I_{\rm X}$ and $\alpha - T_{\rm X}$ relations provide strong evidence that the Abell 2744 halo is a two-component halo. The clear separation between these two components may trace different evolutionary stages of the same phenomenon. Abell 2744 is known to show a very complicated merger dynamics (Merten et al. 2011; Owers et al. 2011; Medezinski et al. 2016; Golovich et al. 2019). Both optical and X-ray analyses point to a violent major merger in the central region along the northsouth axis with a larger line of sight component.

Owers et al. (2011) suggested that some component of the northern subcluster is directed toward the north to northwest. The tight anticorrelation between the radio spectral index and X-ray surface brightness and a moderate positive correlation between the spectral index and ICM temperature in the north to northwest direction favors this. Moreover, Owers et al. (2011) speculated that the small northwestern clump (subcluster 5) is most likely in a post, off-center, core passage phase traveling to the north or northeast. In the $\alpha - I_{\rm X}$ correlation, the data points from subcluster 5 is in line with the detected anticorrelation in the northern part of the halo, which seems to be consistent with the fact that this component may be traveling to the northeast.

In the southern part of the cluster we detected a positive correlation between the spectral index and X-ray surface brightness. If interpreted with turbulent reacceleration models, this suggests that gas dynamics and consequently both the turbulent and magnetic field properties in the dense regions, namely subclusters 2 and 3, are slightly different from the external (less dense) regions and from the northern part of the halo (e.g., Brunetti et al. 2001; Brunetti & Lazarian 2007; Bonafede et al. 2018).

7. Polarization and Faraday rotation

Pearce et al. (2017) found that all four relics in Abell 2744 are highly polarized at 2−4 GHz and show an aligned B-vectors distribution. They presented S-band polarization maps without correcting for Faraday rotation effect. We report here Faraday Rotation Measure (RM) analysis from 1−4 GHz to understand the polarization properties of the relics in the field. For polarization calibration details, we refer to Pearce et al. (2017).

We create Stokes IQU cubes at 10″ resolution. These are only used to study the main relic R1. Because of the radio surface brightness of the components R2, R3, and R4 relative to R1 are very low, these are studied using lower-resolution 15″ Stokes IQU cubes. The imaging was performed with `Briggs` weighing and `robust` = 0.5. As the output images has slightly different resolutions, all images were smoothed to a common resolution, namely 10″ and 15″. Images with poor sensitivity or significant artifact contamination were discarded. The polarization properties are summarized in Table 7.

The resulting polarization intensity maps of the main relic R1 are shown in Fig. 16. The relic is polarized over its

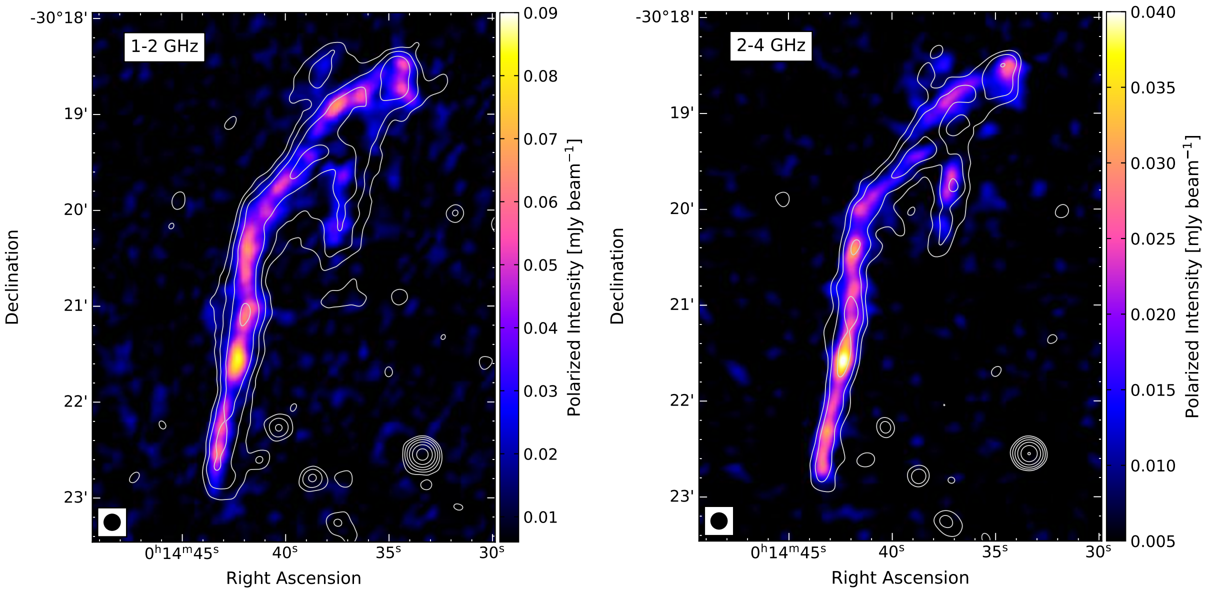

Fig. 16. Polarization intensity images of the main relic R1 at 10″ resolution. The images show that the relic is polarized over its entire length from 1 to 4 GHz. Contour levels are drawn at $[1, 2, 4, 8, \ldots] \times 5\sigma_{\rm rms}$ and are from the Stokes I images. The beam sizes are indicated in the bottom left corner of the each image.

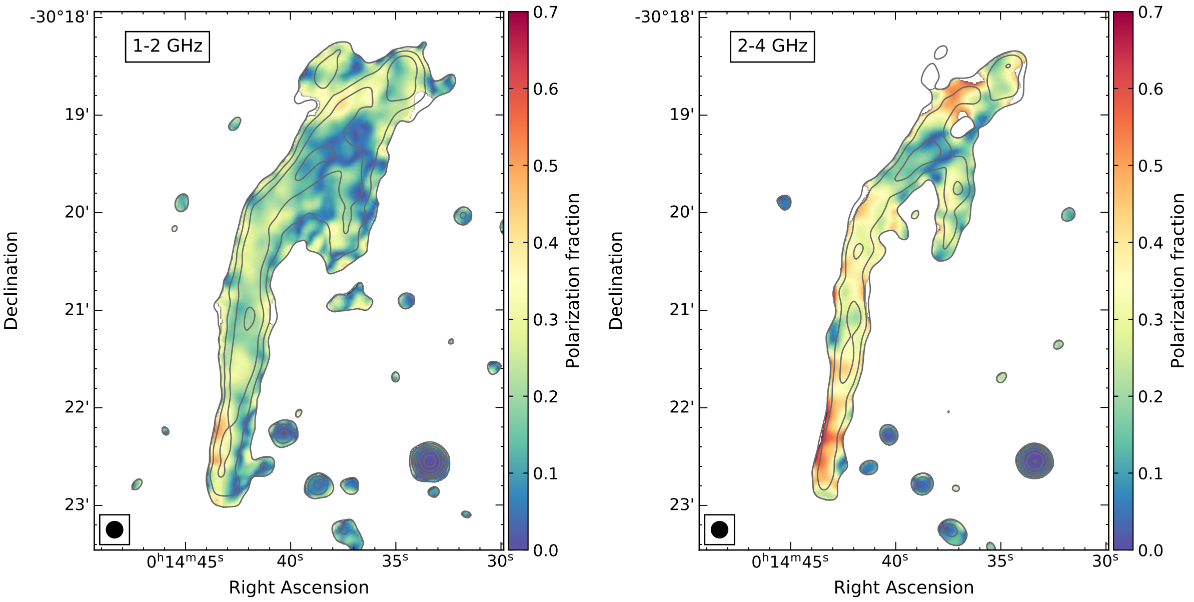

Fig. 17. Fractional polarization maps of the main relic at 10″ resolution. The degree of polarization across the relic decreases when going from S-band (*right*) to L-band (*left*). Some local fluctuations in polarization fraction are visible, particularly in the northern part of the relic. Contour levels are same as in Fig. 16.

entire length in both, the VLA S- and L-band. The morphology of the polarized emission is similar to the total power emission. In Fig. 17, we show the fractional polarization maps at 10″ resolution. The polarization fraction across the relic varies between 2 and 64%, where it can be measured. The spatially averaged polarization fraction over R1 is about 19% at 1−2 GHz and 30% at 2−4 GHz, showing that the degree of polarization decreases significantly with increasing wavelength.

In addition, we observe some local fluctuations in the polarization fraction across the relic, particularly in the northern part of the relic. These local fluctuations are most likely an outcome of a perturbed ICM at the location of the relic.

The beam depolarization could lead to a significant loss of the observed polarized signal. We also measured the polarization fraction from 15″ maps. The resulting values are about 12% lower than those obtained at 10″ resolution. This implies that the intrinsic polarization is very likely higher than reported in Table 7.

At L-band (1−2 GHz), there is tentative evidence to suggest that the high degree of polarization is observed at the eastern edge of the relic (see Fig. 17). This is the area where we expect to witness the fresh acceleration of ICM electrons. In particular, at the northern part of the relic (excluding R1-A), the polarization fraction decreases as we approach the downstream region. Recently, Di Gennaro et al. (2021) found a clear gradient in the

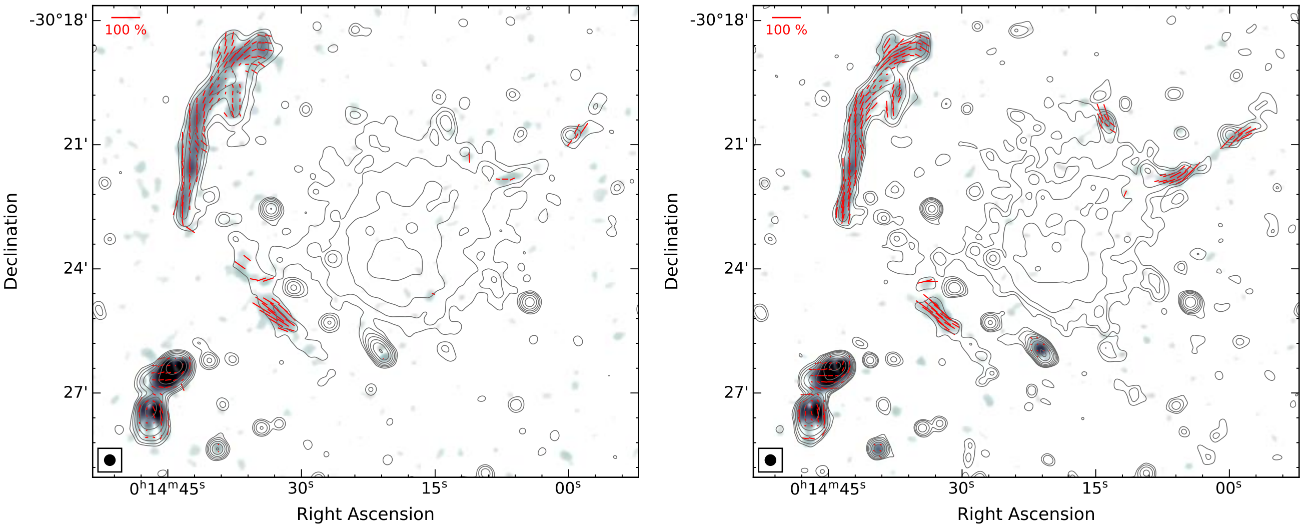

Fig. 18. VLA *L*-band (*left*) and *S*-band (*right*) polarization intensity maps at 15″ resolution. Red lines represent the magnetic field vectors. Their orientation represents the projected magnetic field corrected for Faraday rotation and the contribution from the Galactic foreground. For all four relics, the magnetic-field vectors are uniformly disturbed and parallel to the orientation of the radio emission. The vector lengths is proportional to the polarization percentage. No vectors were drawn for pixels below 3σ. Contour levels are drawn at $[1, 2, 4, 8, \ldots] \times 5\sigma_{\rm rms}$ and are from the Stokes *I* images.

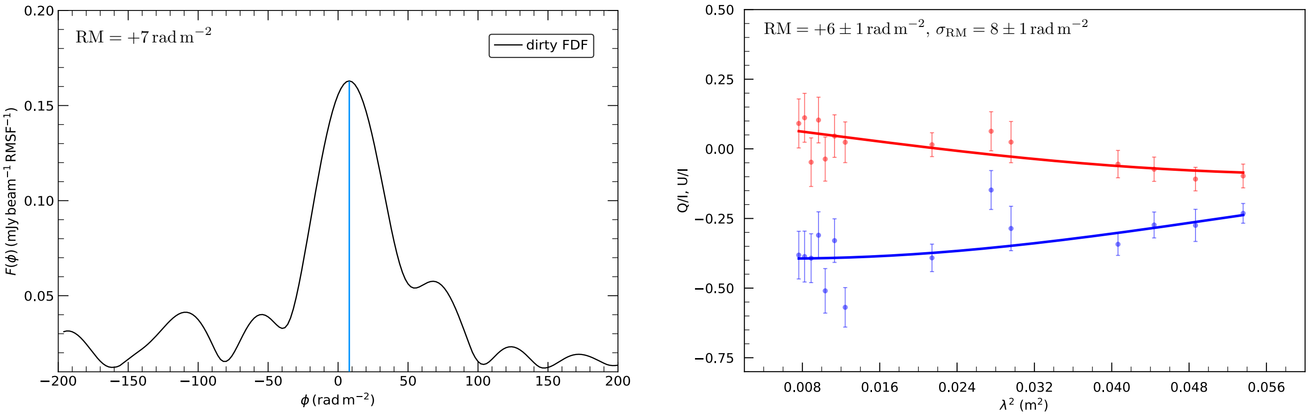

Fig. 19. *Left*: Faraday spectrum of one of the regions within R1 obtained using RM-synthesis. The blue line indicates the peak RM. *Right*: corresponding QU-fitting spectrum fitted with a single RM component and an exponential external depolarization term. The fractional Stokes *Q* (blue) and *U* (red) with the dots showing the observed data points and the solid lines the best-fit model from the QU-fitting. Both RM-synthesis and QU-fitting spectra are consistent with a single RM component that has a low value of Faraday dispersion measure, indicating that the relic R1 is located far outside of the cluster or toward the observer.

polarization fraction across the Sausage relic. They speculated that such a trend is possibly due to projections and/or decrease in the magnetic field anisotropy toward the cluster center. Such trends is expected in the presence of a shocked turbulent ICM (Domínguez-Fernández et al. 2021). On the other hand, if the magnetic field remains regular at the position of the relic, we would expect a polarization fraction increasing toward the downstream of the shock front.

As shown in Fig. 18, R2 and R3 are also highly polarized in *L*-band while no polarized emission is detected for R4. The degree of polarization drops quickly for R3 (from 32% to 13%) and R4 (from 25% to 8%) with increasing wavelength while moderately for R2; see Table 7. As previously reported by Pearce et al. (2017), the magnetic field vectors are strikingly aligned with the orientation of the emission for all relics and even across R1-A. We do not find any small-scale variation in the magnetic field orientation across and along the relics in both the *L* and *S*-band.

RM-synthesis (Brentjens & de Bruyn 2005) was performed on *IQU* cubes with 131 spectral channels using "`pyrmsynth`" code[4]. The RM-cube synthesizes a range of RM from $-200\,\mathrm{rad\,m^{-2}}$ to $+200\,\mathrm{rad\,m^{-2}}$ with a bin size of $1\,\mathrm{rad\,m^{-2}}$. The Faraday spectrum of one of the regions within R1 is shown in the left panel of Fig. 19. The RM across the entire relic is relatively uniform and shows a well-defined single peak.

The mean RM across R1 is about $+8\,\mathrm{rad\,m^{-2}}$. Our own Milky Way contributes to extragalactic RM values. The expected Galactic RM at the location of the cluster is about $6\,\mathrm{rad\,m^{-2}}$ (Oppermann et al. 2012). Therefore, the detected RM's are consistent with the average Galactic foreground.

To analyze the Faraday rotation properties of the emission and of the intervening ICM, we also applied QU-fitting to the main relic R1. Since the relic has a very low surface brightness, to detect the relic with a sufficiently good signal-to-noise

---

[4] `https://github.com/mrbell/pyrmsynth`

in Stokes Q and U we imaged L- and S-band data per spectral window rather than using channel wise Stokes IQU images. We divided the relic into 33 square boxes with width of 10″. As the fractional polarization varies between 1 and 4 GHz, we fit the data with a single RM component and an exponential depolarization term as formulated in Burn (1966).

$$P(\lambda^2) = I_0(\lambda)\, p_0\, e^{2i(\psi_0 + \mathrm{RM}\lambda^2)}\, e^{-2\sigma_{\mathrm{RM}}^2 \lambda^4}, \tag{11}$$

where $P(\lambda^2)$ is the complex polarization as a function of wavelength, I_0 the total intensity of the source, and p_0 is the intrinsic polarization fraction. $\psi_0(\lambda^2)$ is the intrinsic polarization angle, RM is the rotation measure and σ_{RM} is the Faraday dispersion measure of the Gaussian distributed rotation measures.

We performed QU-fitting using the functionality available as part of the `RM-tools` suite[5]. The best-fit is determined by a nested sampling algorithm. The QU-fitted spectrum of one of the regions is shown in the right panel of Fig. 19. A single component in Faraday space with depolarization term provides a good fit, as also seen in the Faraday spectra obtained from RM-Synthesis. The RM mainly varies from +1 to +19 rad m^{-2} across the relic. The σ_{RM} is in the range 3−8 rad m^{-2}. The lower value of Faraday dispersion measure implies that any contribution from the Faraday rotating intervening material is very small and the relic is located far outside the cluster or toward the observer. The σ_{RM} values across R2 and R3 are also low, indicating that both of these relics are located in the low density ICM.

Under a simple hypothesis, Faraday dispersion measure can be used to constrain the magnetic field strength as (Sokoloff et al. 1998)

$$\sigma_{\mathrm{RM}} = \sqrt{(1/3)}\, 0.81\, \langle n_{\mathrm{e}} \rangle\, B\, (L\, t/f)^{0.5}, \tag{12}$$

where $\langle n_{\mathrm{e}} \rangle$ is the average thermal electron density of the ionized gas along the line of sight in cm^{-3}, B is the magnetic field strength in μG, and f is the volume filling factor of the Faraday-rotating gas. L is the path length through the thermal gas and t is the turbulence scale, both in pc. We use $t = 40$ kpc (the RM fluctuations measured from 10″ images), $L = 2.4$ Mpc (the total extent of cluster), and $f = 0.5$ (e.g., Murgia et al. 2004).

At the location of the main relic, the thermal electron density is about 10^{-4} cm^{-3} (Eckert et al. 2016; Botteon et al. 2020b). The highest value of σ_{RM} across the R1 relic is about 8 rad m^{-2}. By inserting all values in Eq. (12), we obtained $B \sim 0.5$ μG.

The polarization analysis suggests that R2 and R3 are located at the cluster outskirts. Both sources show a power-law spectrum, we do not find any hint of curved spectrum between 385 MHz and 3 GHz. In addition, R2 is reported to trace a shock front (Pearce et al. 2017). Based on the morphology, and the spectral and polarization properties we conclude that R2 and R3 are shock related structures. Shock waves generated by cluster mergers can compress AGN fossil radio plasma or fossil plasma can passively evolve from a switched off AGN, producing so called radio phoenices or AGN relics. Both of these sources have relatively small sizes because with time radio plasma losses most of the energetic electrons responsible for the radio emission by radiative energy losses (Enßlin & Gopal-Krishna 2001). Due to the small size, therefore, R4 could be a radio phoenix or AGN relic.

8. Conclusions and summary

In this work, we have presented uGMRT (300−850 MHz) total power and VLA (1−4 GHz) polarization observations of the galaxy cluster Abell 2744. These observations allowed us to perform a detailed spectral and polarization analysis of the diffuse radio emission sources present in this system. To quantify the connection between the thermal and nonthermal components of the intracluster medium, we also combine the radio data with *Chandra* X-ray observations. In our new images, we detect the previously known radio relics R1, R2, R3, and R4, and the radio halo. From these observations we were able to characterize the spectral properties and the radio-versus-X-ray relations of the central halo emission in unprecedented detail. We summarize the overall results as follows:

1. The halo emission is more extended than previously reported, namely ∼2.5 Mpc. The observed total extent of the halo changes with the observing frequency, that is it is more extended toward low frequencies.
2. The radio integrated emission from the entire halo follows a power law spectrum between 150 MHz and 3 GHz and has a slope of $\alpha = -1.14 \pm 0.04$. In contrast, subregions show a slightly different spectra and high frequency steepening. This suggests that an overall power-law spectrum can be observed in combination of a variety of different spectra.
3. The spatially resolved spectral index maps of the halo show the presence of localized regions in which the spectral index is significantly different from the average. The spectral index in the innermost regions is relatively flat and steepens in the outer regions. This is consistent with the turbulent (re-)acceleration models, assuming that there is more dissipated turbulent kinetic power or a higher magnetic magnetic field strength in the innermost halo region. We find a mean scatter of 0.24 around the mean spectral index of −1.15 between 675 MHz and 3.0 GHz, suggesting small-scale spectral index fluctuations across the halo.
4. The spatially resolved map also reveals spectral curvature across the halo. The spectral shapes inferred from spatially resolved map show regions with a complex curvature distribution.
5. The radio brightness of the halo strongly correlates with the X-ray brightness at all observed frequencies. The slopes of the correlation remains remarkably uniform at 675 MHz, 1.5 GHz, and 3 GHz, namely 0.74 ± 0.02. In addition, the correlation slope across the southern part of the halo is significantly steeper than the northern part of the halo.
6. The point-to-point comparison between the X-ray surface brightness and spectral index across the halo reveals two different trends. We find a strong anticorrelation in the northern part of the halo and a positive correlation in the southern part of the halo. This suggests that the radio halo indeed consists of two major components, with distinct evolutionary signatures.
7. The point-to-point comparison between the spectral index and the ICM temperature also shows two different trends. This further strengthens the fact that the halo has at least two different components. We find a moderate positive correlation between these two quantities in the northern part of the halo.
8. The integrated radio spectrum of the main relic, R1, follows a simple power-law between 150 MHz and 3 GHz. The spectral index for the main relic R1 is −1.17 ± 0.04. The radio spectra suggest a shock with Mach number 3.6 which is intriguingly consistent with the X-ray shock Mach number ($\mathcal{M} = 3.7 \pm 0.4$) obtained from the temperature jump at the location of the relic, and is disagreement with previous X-ray estimates of the shock strength based on the density jump. If CRe are accelerated from the thermal pool, a

---

[5] https://github.com/CIRADA-Tools/RM

   plausible acceleration efficiency below 1% results in the observed radio power of the relic R1 if a large fraction of the shock front has a strength obtained from the integrated spectrum and the magnetic field strength is of a few µG or stronger.
9. The other three fainter relics also follow a power-law between 385 MHz and 3 GHz. We obtained spectral indices of $\alpha_{\rm int, R2} = -1.19 \pm 0.05$, $\alpha_{\rm int, R3} = -1.10 \pm 0.05$, and $\alpha_{\rm int, R4} = -1.14 \pm 0.04$. For all four relics in the Abell 2744 field, the integrated spectral index values suggest shocks with Mach number in the range 3.3–4.5. This suggests that the integrated radio spectra of relics may be always dominated by high Mach number shocks as found in simulations (Wittor et al. 2019; Dominguez-Fernandez et al. 2020), irrespective of radio brightness. Our results also suggests that the properly derived integrated spectral indices are in the −1.0 to −1.2 range, implying that a tail in the Mach distribution determines the integrated spectral index.
10. Relics R1, R2, and R3 are highly polarized between 1 and 4 GHz and show a single RM component. The mean RMs in these three relics are very close to the Galactic foreground. The Faraday dispersion is below 10 rad m^{-2}, indicating very little Faraday-rotating intervening material along the line of sight. This suggest that R1, R2, and R3 are located in regions of low density ICM, toward the observer.

The presence of curved spectra in the halo subregions, the spectral index fluctuations, the steep spectral indices in the outermost regions, a hint of spectral curvature, and the sublinear $I_{\rm R}$–$I_{\rm X}$ correlation slope is in line with turbulent reacceleration models for the origin of radio emitting electrons. The high quality data from the uGMRT and the VLA suggests that we are entering into a new level of complexity in radio halos. Our findings highlight that the combination of two or more components may result in an overall power-law spectrum in radio halos.

In conclusion, the emerging complexity in the distribution of nonthermal components in Abell 2744 echoes the richness of dynamical structures highlighted by optical and X-ray studies (e.g., Owers et al. 2011; Merten et al. 2011; Hattori et al. 2017; Golovich et al. 2019), and this hints at a multiple-merger scenario for this system. Different episodes of matter accretions, following the infall along the multiple filaments revealed by X-ray and lensing studies (Eckert et al. 2016; Jauzac et al. 2018), are likely to explain also the unusual variety of radio structures in Abell 2744, making it a remarkable laboratory to study the interplay between thermal and nonthermal energy components of the ICM.

Acknowledgements. We thank Nicola Locatelli for helpful discussion. KR, FV, and PDF acknowledge financial support from the ERC Starting Grant "MAGCOW", no. 714196. RJvW acknowledges support from the ERC Starting Grant-ClusterWeb 804208. CJR, MB, EB, and AB acknowledge financial support from the ERC Starting Grant "DRANOEL", number 714245. WF acknowledges support from the Smithsonian Institution and the *Chandra* High Resolution Camera Project through NASA contract NAS8-03060. DW is funded by the Deutsche Forschungsgemeinschaft (DFG, German Research Foundation)-441694982. This research made use of computer facility at IRA Bologna, Italy, Thüringer Landessternwarte, Tautenburg, Germany, and the HPC resources at the Physical Research Laboratory (PRL), India. We thank the staff of the GMRT that made these observations possible. GMRT is run by the National Centre for Radio Astrophysics of the Tata Institute of Fundamental Research. The National Radio Astronomy Observatory is a facility of the National Science Foundation operated under cooperative agreement by Associated Universities. The scientific results reported in this article are based in part on observations made by the *Chandra* X-ray Observatory and published previously in Pearce et al. (2017). Finally, we wish to acknowledge the developers of the following python packages, which were used extensively during this project: `aplpy` (Robitaille & Bressert 2012), `astropy` (Astropy Collaboration 2013), `matplotlib` (Hunter 2007), `numpy` (van der Walt et al. 2011) and `scipy` (Jones et al. 2001).

References

Adam, R., Goksu, H., Brown, S., Rudnick, L., & Ferrari, C. 2021, A&A, 648, A60
Akamatsu, H., Takizawa, M., Nakazawa, K., et al. 2012, PASJ, 64, 67
Astropy Collaboration (Robitaille, T. P., et al.) 2013, A&A, 558, A33
Blasi, P., & Colafrancesco, S. 1999, Astropart. Phys., 12, 169
Bonafede, A., Brüggen, M., van Weeren, R., et al. 2012, MNRAS, 426, 40
Bonafede, A., Intema, H. T., Brüggen, M., et al. 2014, ApJ, 785, 1
Bonafede, A., Brüggen, M., Rafferty, D., et al. 2018, MNRAS, 478, 2927
Bonafede, A., Brunetti, G., Vazza, F., et al. 2021, ApJ, 907, 32
Botteon, A., Gastaldello, F., Brunetti, G., & Kale, R. 2016, MNRAS, 463, 1534
Botteon, A., Gastaldello, F., & Brunetti, G. 2018, MNRAS, 476, 5591
Botteon, A., Brunetti, G., van Weeren, R. J., et al. 2020a, ApJ, 897, 93
Botteon, A., Brunetti, G., Ryu, D., & Roh, S. 2020b, A&A, 634, A64
Brentjens, M. A., & de Bruyn, A. G. 2005, A&A, 441, 1217
Brunetti, G., & Jones, T. W. 2014, Int. J. Mod. Phys. D, 23, 1430007
Brunetti, G., & Lazarian, A. 2007, MNRAS, 378, 245
Brunetti, G., & Lazarian, A. 2016, MNRAS, 458, 2584
Brunetti, G., Setti, G., Feretti, L., & Giovannini, G. 2001, MNRAS, 320, 365
Brunetti, G., Zimmer, S., & Zandanel, F. 2017, MNRAS, 472, 1506
Bruno, L., Rajpurohit, K., Brunetti, G., et al. 2021, A&A, 650, A44
Burn, B. J. 1966, MNRAS, 133, 67
Cassano, R., & Brunetti, G. 2005, MNRAS, 357, 1313
Cassano, R., Brunetti, G., & Setti, G. 2006, MNRAS, 369, 1577
Chandra, P., Ray, A., & Bhatnagar, S. 2004, ApJ, 612, 974
Cova, F., Gastaldello, F., Wik, D. R., et al. 2019, A&A, 628, A83
de Gasperin, F., van Weeren, R. J., Brüggen, M., et al. 2014, MNRAS, 444, 3130
de Gasperin, F., Brunetti, G., Brüggen, M., et al. 2020, A&A, 642, A85
Dennison, B. 1980, ApJ, 239, L93
Di Gennaro, G., van Weeren, R. J., Hoeft, M., et al. 2018, ApJ, 865, 24
Di Gennaro, G., van Weeren, R. J., Rudnick, L., et al. 2021, ApJ, 911, 3
Dolag, K., & Enßlin, T. A. 2000, A&A, 362, 151
Dominguez-Fernandez, P., Bruggen, M., Vazza, F., et al. 2020, MNRAS, 500, 795
Domínguez-Fernández, P., Brüggen, M., Vazza, F., et al. 2021, MNRAS, 507, 2714
Ebeling, H., Edge, A. C., Mantz, A., et al. 2010, MNRAS, 407, 83
Eckert, D., Jauzac, M., Vazza, F., et al. 2016, MNRAS, 461, 1302
Enßlin, T. A., & Gopal-Krishna 2001, in Particles and Fields in Radio Galaxies Conference, eds. R. A. Laing, & K. M. Blundell, ASP Conf. Ser., 250, 454
Enßlin, T. A., Biermann, P. L., Klein, U., & Kohle, S. 1998, A&A, 332, 395
Enßlin, T., Pfrommer, C., Miniati, F., & Subramanian, K. 2011, A&A, 527, A99
Feretti, L., Fusco-Femiano, R., Giovannini, G., & Govoni, F. 2001, A&A, 373, 106
Feretti, L., Giovannini, G., Govoni, F., & Murgia, M. 2012, A&ARv, 20, 54
George, L. T., Dwarakanath, K. S., Johnston-Hollitt, M., et al. 2017, MNRAS, 467, 936
Giovannini, G., Tordi, M., & Feretti, L. 1999, New Astron., 4, 141
Golovich, N., Dawson, W. A., Wittman, D. M., et al. 2019, ApJ, 882, 69
Govoni, F., Enßlin, T. A., Feretti, L., & Giovannini, G. 2001a, A&A, 369, 441
Govoni, F., Feretti, L., Giovannini, G., et al. 2001b, A&A, 376, 803
Hattori, S., Ota, N., Zhang, Y.-Y., Akamatsu, H., & Finoguenov, A. 2017, PASJ, 69, 39
Hindson, L., Johnston-Hollitt, M., Hurley-Walker, N., et al. 2014, MNRAS, 445, 330
Hoang, D. N., Shimwell, T. W., Stroe, A., et al. 2017, MNRAS, 471, 1107
Hoang, D. N., Shimwell, T. W., van Weeren, R. J., et al. 2019, A&A, 622, A20
Hoeft, M., & Brüggen, M. 2007, MNRAS, 375, 77
Hunter, J. D. 2007, Comput. Sci. Eng., 9, 90
Intema, H. T., van der Tol, S., Cotton, W. D., et al. 2009, A&A, 501, 1185
Jaffe, W. J., & Perola, G. C. 1973, A&A, 26, 423
Jauzac, M., Eckert, D., Schaller, M., et al. 2018, MNRAS, 481, 2901
Jones, E., Oliphant, T., Peterson, P., et al. 2001, SciPy: Open Source Scientific Tools for Python, `http://www.scipy.org`
Kang, H. 2015, J. Korean Astron. Soc., 48, 9
Kang, H., & Ryu, D. 2011, ApJ, 734, 18
Kang, H., & Ryu, D. 2016, ApJ, 823, 13
Kang, H., Ryu, D., & Jones, T. W. 2012, ApJ, 756, 97
Katz-Stone, D. M., Rudnick, L., & Anderson, M. C. 1993, ApJ, 407, 549
Kelly, B. C. 2007, ApJ, 665, 1489
Kempner, J. C., & David, L. P. 2004, MNRAS, 349, 385
Kierdorf, M., Beck, R., Hoeft, M., et al. 2017, A&A, 600, A18
Komissarov, S. S., & Gubanov, A. G. 1994, A&A, 285, 27

Limousin, M., Richard, J., Jullo, E., et al. 2016, A&A, 588, A99
Locatelli, N. T., Rajpurohit, K., Vazza, F., et al. 2020, MNRAS, 496, L48
Mantz, A., Allen, S. W., Ebeling, H., Rapetti, D., & Drlica-Wagner, A. 2010, MNRAS, 406, 1773
Markevitch, M., & Vikhlinin, A. 2001, ApJ, 563, 95
Markevitch, M., Govoni, F., Brunetti, G., & Jerius, D. 2005, ApJ, 627, 733
Medezinski, E., Umetsu, K., Okabe, N., et al. 2016, ApJ, 817, 24
Merten, J., Coe, D., Dupke, R., et al. 2011, MNRAS, 417, 333
Murgia, M., Govoni, F., Feretti, L., et al. 2004, A&A, 424, 429
Nuza, S. E., Gelszinnis, J., Hoeft, M., & Yepes, G. 2017, MNRAS, 470, 240
Oppermann, N., Junklewitz, H., Robbers, G., et al. 2012, A&A, 542, A93
Orrú, E., Murgia, M., Feretti, L., et al. 2007, A&A, 467, 943
Owen, F. N., Rudnick, L., Eilek, J., et al. 2014, ApJ, 794, 24
Owers, M. S., Randall, S. W., Nulsen, P. E. J., et al. 2011, ApJ, 728, 27
Pacholczyk, A. G. 1970, Radio Astrophysics. Nonthermal Processes in Galactic and Extragalactic Sources (San Francisco: W. H. Freeman)
Paul, S., Salunkhe, S., Datta, A., & Intema, H. T. 2019, MNRAS, 489, 446
Pearce, C. J. J., van Weeren, R. J., Andrade-Santos, F., et al. 2017, ApJ, 845, 81
Petrosian, V. 2001, ApJ, 557, 560
Pfrommer, C., Enßlin, T. A., & Springel, V. 2008, MNRAS, 385, 1211
Pinzke, A., Oh, S. P., & Pfrommer, C. 2013, MNRAS, 435, 1061
Pinzke, A., Oh, S. P., & Pfrommer, C. 2017, MNRAS, 465, 4800
Rajpurohit, K., Hoeft, M., van Weeren, R. J., et al. 2018, ApJ, 852, 65
Rajpurohit, K., Hoeft, M., Vazza, F., et al. 2020a, A&A, 636, A30
Rajpurohit, K., Vazza, F., Hoeft, M., et al. 2020b, A&A, 642, L13
Rajpurohit, K., Brunetti, G., Bonafede, A., et al. 2021a, A&A, 646, A135
Rajpurohit, K., Wittor, D., van Weeren, R. J., et al. 2021b, A&A, 646, A56
Robitaille, T., & Bressert, E. 2012, Astrophysics Source Code Library [record ascl:1208.017]
Roh, S., Ryu, D., Kang, H., Ha, S., & Jang, H. 2019, ApJ, 883, 138
Rudnick, L., Katz-Stone, D. M., & Anderson, M. C. 1994, ApJS, 90, 955
Sarazin, C. L. 2002, in The Physics of Cluster Mergers, eds. L. Feretti, I. M. Gioia, & G. Giovannini, 272, 1
Scaife, A. M. M., & Heald, G. H. 2012, MNRAS, 423, L30
Shimwell, T. W., Brown, S., Feain, I. J., et al. 2014, MNRAS, 440, 2901
Shimwell, T. W., Markevitch, M., Brown, S., et al. 2015, MNRAS, 449, 1486
Skillman, S. W., Xu, H., Hallman, E. J., et al. 2013, ApJ, 765, 21
Sokoloff, D. D., Bykov, A. A., Shukurov, A., et al. 1998, MNRAS, 299, 189
Storm, E., Jeltema, T. E., & Rudnick, L. 2015, MNRAS, 448, 2495
Struble, M. F., & Rood, H. J. 1999, ApJS, 125, 35
Stuardi, C., Bonafede, A., Wittor, D., et al. 2019, MNRAS, 489, 3905
Thierbach, M., Klein, U., & Wielebinski, R. 2003, A&A, 397, 53
Trasatti, M., Akamatsu, H., Lovisari, L., et al. 2015, A&A, 575, A45
Vacca, V., Feretti, L., Giovannini, G., et al. 2014, A&A, 561, A52
van der Walt, S., Colbert, S. C., & Varoquaux, G. 2011, Comput. Sci. Eng., 13, 22
van Weeren, R. J., Röttgering, H. J. A., Brüggen, M., & Hoeft, M. 2010, Science, 330, 347
van Weeren, R. J., Röttgering, H. J. A., Rafferty, D. A., et al. 2012a, A&A, 543, A43
van Weeren, R. J., Röttgering, H. J. A., Intema, H. T., et al. 2012b, A&A, 546, A124
van Weeren, R. J., Brunetti, G., Brüggen, M., et al. 2016, ApJ, 818, 204
van Weeren, R. J., Andrade-Santos, F., Dawson, W. A., et al. 2017, Nat. Astron., 1, 0005
van Weeren, R. J., de Gasperin, F., Akamatsu, H., et al. 2019, Space Sci. Rev., 215, 16
Venturi, T., Giacintucci, S., Dallacasa, D., et al. 2013, A&A, 551, A24
Wittor, D., Hoeft, M., Vazza, F., Brüggen, M., & Domínguez-Fernández, P. 2019, MNRAS, 490, 3987
Wittor, D., Ettori, S., Vazza, F., et al. 2021, MNRAS, 506, 396
Xie, C., van Weeren, R. J., Lovisari, L., et al. 2020, A&A, 636, A3